nature electronics

Article

https://doi.org/10.1038/s41928-023-01071-2

Strain engineering of vertical molybdenum ditelluride phase-change memristors

Received: 22 February 2023

Accepted: 13 October 2023

Published online: 23 November 2023

Check for updates

Wenhui Hou ® ^{1,4}, Ahmad Azizimanesh ^{1,4}, Aditya Dey ® ², Yufeng Yang ¹, Wuxiucheng Wang ® ¹, Chen Shao ¹, Hui Wu ® ¹, Hesam Askari ® ², Sobhit Singh ® ² & Stephen M. Wu ® ^{1,3} ⋈

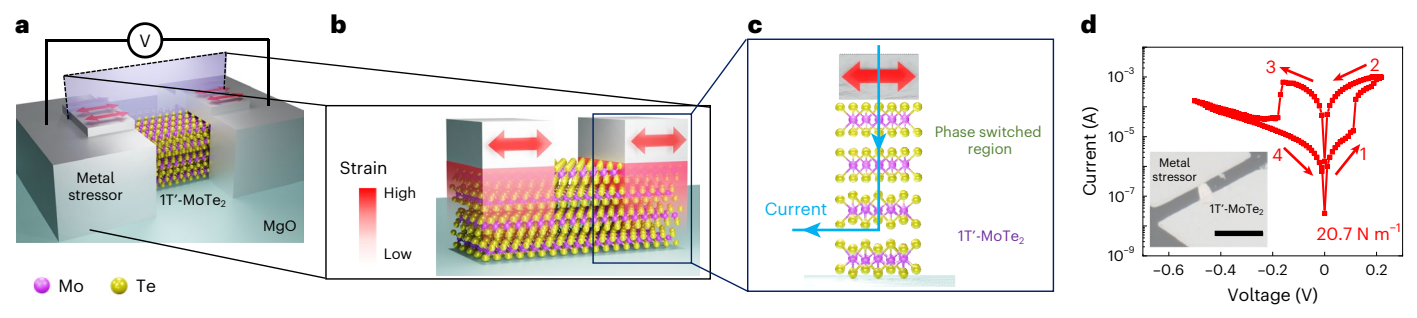
Electric-field-controlled electronic and structural phase transitions can be used as a mechanism for memristive switching in two-dimensional (2D) materials. However, such 2D phase-change memristors do not typically outperform other 2D memristors. Here we report high-performance bipolar phase-change memristors that are based on strain-engineered multilayer molybdenum ditelluride (MoTe₂). Using process-induced strain engineering, stressed metal thin films are patterned into contacts that induce a strain-driven semimetallic-to-semiconducting phase transition in the MoTe₂, forming a self-aligned vertical transport memristor with semiconducting MoTe₂ as the active region. By using strain to bring the material close to the phase transition boundary, the devices can exhibit switching voltages of 90 mV, on/off ratios of 10^8 , switching times of 5 ns and retentions of over 10^5 s. A single-process parameter, contact metal film force (the product of the film stress and film thickness), can be varied to tune the device switching voltage and on/off ratio.

Memristors are two-terminal-resistive switches that can be switched between a high resistance state (HRS) and a low resistance state (LRS) under applied voltage biases^{1,2}, and are of potential use in next-generation memory and neuromorphic computation^{3,4}. Memristors based on two-dimensional (2D) materials are of particular interest due to their atomically thin structure, which leads to high-performance metrics such as fast switching at low power, high scalability and compatibility with flexible substrates^{5,6}. However, despite advances⁷⁻¹⁹, there still remains a gap between 2D memristors and the highest performing memristive switching devices based on other materials. This gap results from the typical mechanism of operation: filamentary conduction from the motion of defects, grain boundaries or metal ions. This is the same mechanism as most other memristors, and in 2D materials, it leads to many of the same fundamental limitations in device performance, such as needing forming steps, having high switching voltages or low on/off ratios, and having highly variable device characteristics that cannot be engineered by design.

One approach to avoid these limitations is to change the mechanism of memristive switching away from filamentary conduction. Recent work has shown that electric-field-induced phase transitions can occur in 2D molybdenum ditelluride (MoTe₂)^{12,20}, which can switch between semiconducting (2H) and semimetallic (1T') phases in a two-terminal memristive device; this approach takes advantage of MoTe₂ being the transition metal dichalcogenide (TMD) with the lowest energy difference between the different structural/electronic phases²¹. However, the performance of phase-change 2D memristors has not exceeded the performance of devices based on the filamentary conduction mechanism for memristive switching.

In this Article, we report a process-induced strain-engineering technique to create single-step self-aligned phase-change memristors based on multilayer $MoTe_2$. Strain is applied to $MoTe_2$ on a device-to-device basis by the contact metal to bias the active region closer to the phase switching point. This lowers the energy difference between the semimetallic and semiconducting structural states of the material, and thus a smaller electric field is needed to achieve

¹Department of Electrical and Computer Engineering, University of Rochester, Rochester, NY, USA. ²Department of Mechanical Engineering, University of Rochester, Rochester, NY, USA. ⁴These authors contributed equally: Wenhui Hou, Ahmad Azizimanesh. —e-mail: stephen.wu@rochester.edu



 $\label{lem:problem} \textbf{Fig. 1} | \textbf{Strain-based 1T'-MoTe}_2 \ memristor. \ a, \ \text{Device schematic showing} \\ \text{stressed contact metals to MoTe}_2, \ with purple plane representing a device cross section. \ b, Cross section of the device in \ a \ with the strain profile. \ c, \ Mechanism of operation for self-aligned vertical transport based on phase-switched MoTe}_2$

directly beneath the contact metal. Double-headed red arrows in a-c represent the uniaxial edge strain effect. d, Typical resistive switching $\emph{I-V}$ characteristic of the strain-based 1T'-MoTe $_2$ memristor. Inset, optical micrograph of the device. Scale bar, $10~\mu m$.

the same memristive switching. The memristors exhibit switching voltages of 90 mV, on/off ratios of 10^8 , switching times of 5 ns, switching energies of 150 aJ and retentions of over 10^5 s, in a bipolar switching non-volatile configuration. Our best single device exhibits an on/off ratio and switching voltage of 7.4×10^7 and 90 mV, respectively. The device parameters (switching voltage, on/off ratio) can also be tuned with a single-process variable—contact metal film force (film stress × film thickness). The overall memristor performance is good compared to 2D and non-2D memristive technologies due to its combination of low voltage switching, high on/off ratios and fast bipolar (non-volatile) switching, as well as moderately high endurance and retention properties.

Device design of strain-based MoTe, memristor

Our approach uses process-induced strain-engineering techniques, adopted from the strain-engineering techniques that have been in standard use in commercial complementary metal-oxide-semiconductor nanofabrication processes. These techniques have been used since the 90 nm technology node in 2003 to selectively enhance the mobility of electrons or holes for n-type metal-oxide-semiconductor (NMOS) or p-type metal-oxide-semiconductor (PMOS) field effect transistor devices with uniaxial tensile or compressive strain, respectively. Highly stressed thin films, such as SiN_x, are selectively deposited on each transistor where the stress of the film relaxes to induce strain in each transistor channel^{22,23}. This same strain-engineering technique can be used on 2D materials, based on thin film stress capping layers, as a scalable way to apply strain to 2D materials on a device-to-device $basis ^{24-27}. \, By \, controlling \, the \, film \, force \, (film \, stress \times film \, thickness) \, and \,$ the geometry of the thin film stressor, it has been shown that both the magnitude²⁶ and the direction²⁵ of the strain can be controlled. This is done in a defect-free single-step deposition process, where the strain has been shown to be stable for months to years²⁷.

In our device design, uniaxial tensile strain is applied by a stressed metallic thin film which doubles as the contact metal for the MoTe₂ device (Fig. 1a). Process-induced strain from the metal contacts is transferred from the top down through van der Waals interaction to the underlying 1T'-MoTe₂ flake (Fig. 1b), as determined by our previous works on the topic^{24-26,28}. Here, this uniaxial strain induces a phase transition underneath the contacts from the semimetallic state to the semiconducting state in a natural vertical transport configuration (Fig. 1c). Thus, with a single-process step, we create a self-aligned phase-change memristor structure identical to the original work¹² on the topic (see Methodsfor more details on the fabrication). Since strain is used to induce the phase transition, it is necessarily close to the phase transition point, where small amounts of perturbation from an electric field applied out-of-plane from an applied two-terminal voltage can now induce the phase transition. This concept was previously used by our group to create a three-terminal MoTe₂ phase-change transistor that operated on gate-controllable strain from a piezoelectric substrate²⁴. In that case, process-induced strain from the contacts was used to bias the device to the most strain sensitive point before piezoelectric strain was used as the trigger to switch the device between two non-volatile phases. Here, we use the same strain-biasing technique, but the trigger is an applied electric field in a two-terminal memristor geometry.

Strain-based resistive switching

Figure 1d shows the typical non-volatile bipolar resistive switching *I–V* characteristic of a strain-based 1T'-MoTe₂ memristor under 20.7 N m⁻¹ film force, where film force (film stress × thickness) is directly proportional to the amount of strain applied from the metal contacts to the flake, as determined by previous works on the topic^{26,29}. The device starts at a HRS due to the Schottky barrier formed between the metal contact and the phase-switched semiconducting layers. When the voltage between the two metal contacts reaches 110 mV, the current suddenly increases and the device enters a LRS. This is because the electric field across the semiconducting layers is large enough to switch them back to the semimetallic state, similar to previous vertical 2H-MoTe₂ $memristor\,works^{12,20}.\,Next, by\,applying\,a\,negative\,voltage\,of\,approximation and the state of approximation and the stat$ mately -160 mV between the two metal contacts, the device switches back to the HRS. So, in our devices, the strain-induced phase transition of MoTe₂ and the electric-field-induced phase transition of MoTe₂ work together in the device switching process, with the former defining the initial semiconducting layers and the latter switching those layers back and forth between the semimetallic and semiconducting phase. This bipolar resistive switching characteristic is repeatable, and no forming process is required. As a control, when devices were made with pure Ag contacts containing low film force (-1.2 N m⁻¹), the devices always show low resistance and the I-V curve always shows a linear dependence with high current value, as shown in Supplementary Fig. 1, indicating the MoTe₂ flake stayed in the 1T' semimetallic state.

Strain profile in the device

To understand how in-plane strain is transferred from the metal contacts to the MoTe₂ flake from the interface down through the entire thickness of the flake, we performed Raman measurements on various flakes with different thickness (Fig. 2a), similar to our previous works on process-induced strain on MoS₂ and 2H-MoTe₂ (refs. 26,28). Tensile transparent thin film stressors (Ti/MgF₂/Al₂O₃ or Al₂O₃/MgF₂/Al₂O₃) with 55 N m⁻¹ film force were used to uniformly cover the flakes of different thickness, which enables us to apply in-plane biaxial strain to the flakes^{26,28} and also leaves those same flakes ready to probe through Raman spectroscopic analysis (Fig. 2b). The A⁵_g (266 cm⁻¹) Raman peak was used to characterize strain, which is a peak shown to be sensitive to strain applied in-plane in the armchair direction of 1T'-MoTe₂(refs. 30,31). As shown by the positive A⁵_g peak shift in Fig. 2c, we found when uniformly covered by tensile stressed

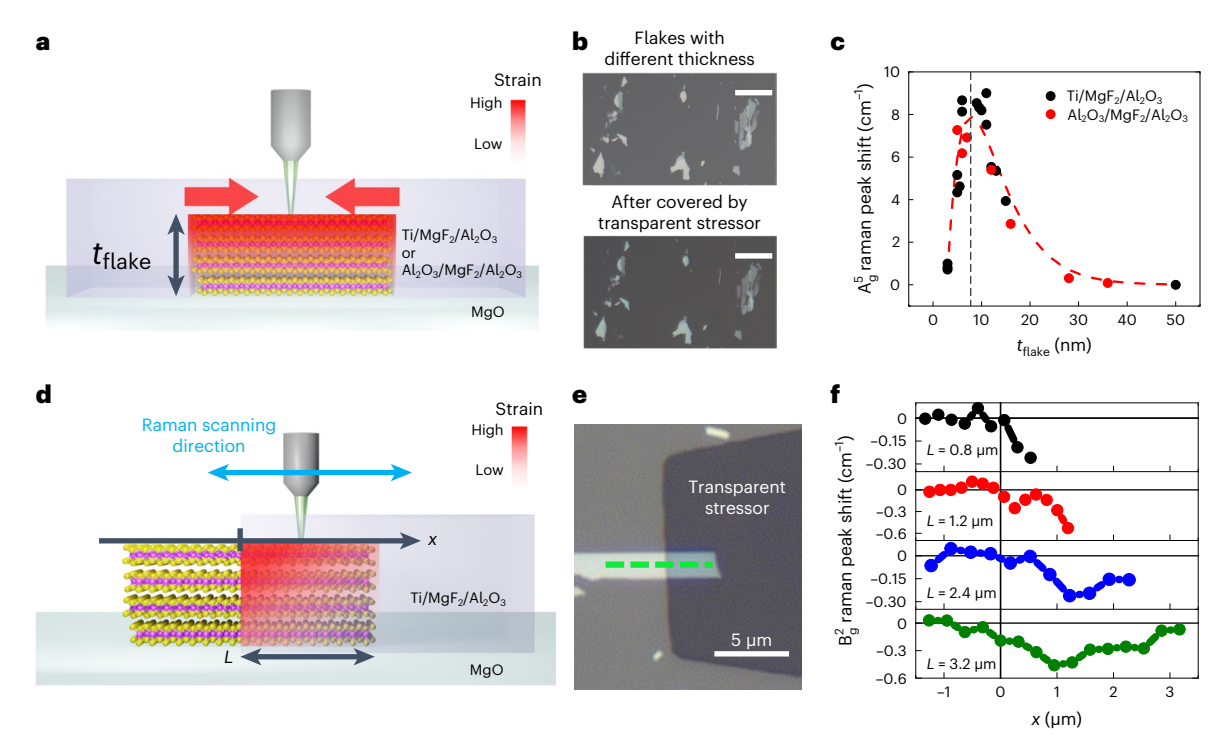


Fig. 2 | **Out-of-plane and in-plane strain profile under the stressor. a**, Schematic showing single-point Raman measurement setup for out-of-plane strain profile characterization, with variable flake thickness (t_{flake}). **b**, Optical microscope image for the MoTe₂ flakes before and after encapsulation by the transparent stressor. Scale bar, $10 \, \mu m. \, c$, A_g^5 (266 cm⁻¹) Raman peak shift of MoTe₂

flakes with different thickness under transparent stressors. d, Schematic showing

Raman line-scan measurements setup for in-plane strain profile characterization, with variable contact length. Position along scan path is denoted by $x.\,e$, Optical microscope image of a MoTe $_2$ flake partially covered by the transparent stressor in the same geometry as contact metals for devices shown in Fig.1d. Green dotted line shows the Raman line-scan path. f, B_g^2 (105 cm $^{-1}$) Raman peak shift line-scan profile across the stressor edge for flakes with different contact length.

thin films, there is compressive strain in the MoTe₂ flake, because the thin film stressor layer relieves its tensile stress by shrinking in all directions^{26,28}. And more importantly, the largest peak shift was observed on flakes with ~7 nm thickness. Thinner flakes showed smaller peak shift because the bottom layers are clamped by the substrate and cannot be fully strained, an effect that was previously shown by our work in MoS₂(ref. 26). Peak shift of flakes with thickness larger than 7 nm also showed exponential decay because of the finite strain transfer length scale in the out-of-plane direction of 1T'-MoTe₂ (~7 nm) and the measured Raman signal is the result of the superimposed Raman signature from highly strained layers of the top 7 nm and the unstrained layers more than 7 nm away from the top. This finite strain transfer length scale effect is present in all 2D materials, but the length is different between different 2D systems depending on interlayer adhesion^{26,28}. It is worth noting from Fig. 2c that points measured from flakes covered by different stressors (Ti/MgF₂/Al₂O₃ or Al₂O₃/MgF₂/Al₂O₃) can be fit with the same curve, which shows that different stressors with the same film force can apply similar amounts of strain to the covered flake26.

To understand how strain is transferred from the metal contacts to the MoTe $_2$ flake along the length of the contact, we performed Raman line scans on various flakes with a 10 nm thickness and different contact length L, as defined in Fig. 2d. These transparent stressors mimic the geometry of our metallic stressors, allowing us to measure the strain profile applied in this type of contact geometry. Tensile transparent stressors (Ti/MgF $_2$ /Al $_2$ O $_3$) with 10 N m $^{-1}$ film force were used to partially cover the flake, with the stressor edge perpendicular to the zigzag direction of the flake (Fig. 2e). The B_g^2 (105 cm $^{-1}$) Raman peak was used to characterize the strain, which is a peak shown to be sensitive to strain applied in the zigzag direction of 1T'-MoTe $_2$ (refs. 30,31). As shown by the negative B_g^2 peak shift in Fig. 2f, we found when partially covered by tensile thin films, there is tensile strain in

the MoTe₂ flake near the stressor's edge, because the edge tends to shrink in the direction perpendicular to itself, which stretches the underlying flake along its zigzag direction. This matches our expectations from our previous works on patterned stressor geometries on MoS₂(ref. 25). Compressive strain along the armchair direction of the flake has also been observed, demonstrated by the positive shift of its A_{α}^{5} peak (Supplementary Fig. 2), resulting from the positive Poisson ratio of the flake³². The relative magnitude of compression along the armchair direction to tension along the zigzag depends on the geometry of our exfoliated flakes, which vary from device to device. A more detailed analysis of these strain profiles is included in Supplementary Figs. 7–14. Our results show that the edge-induced strain from tensile thin film stressors is directional, which applies tensile strain to the underlying flake in the direction perpendicular to the stressor's edge and applies compressive strain to the flake along the stressor's edge, matching our expectation from previous results on MoS_2 (ref. 25). When the contact length L increases to 3.2 µm, the magnitude of the B_g^2 peak shift and the A_g^5 peak shift first increases and reaches a maximum at around 1 μm away from the edge, then gradually decreases and drops back to 0 when it is 3.2 µm away from the edge. This shows that the edge-induced strain is localized near the edge and decreases quickly when it is away from the edge²⁵. Stressors with higher film force (30 N m⁻¹) also shows similar in-plane strain transfer profiles (Supplementary Fig. 3). More detailed information about the strain component specific effect on the phase change, as measured through Raman spectroscopy, is included in Supplementary Figs. 7–14.

Effect of process parameters on devices

With the knowledge of the strain profile in the flake underneath the thin film stressor, we varied different device process parameters and performed a statistical analysis on how these device parameters affect two-terminal electrical device characteristics (Fig. 3).

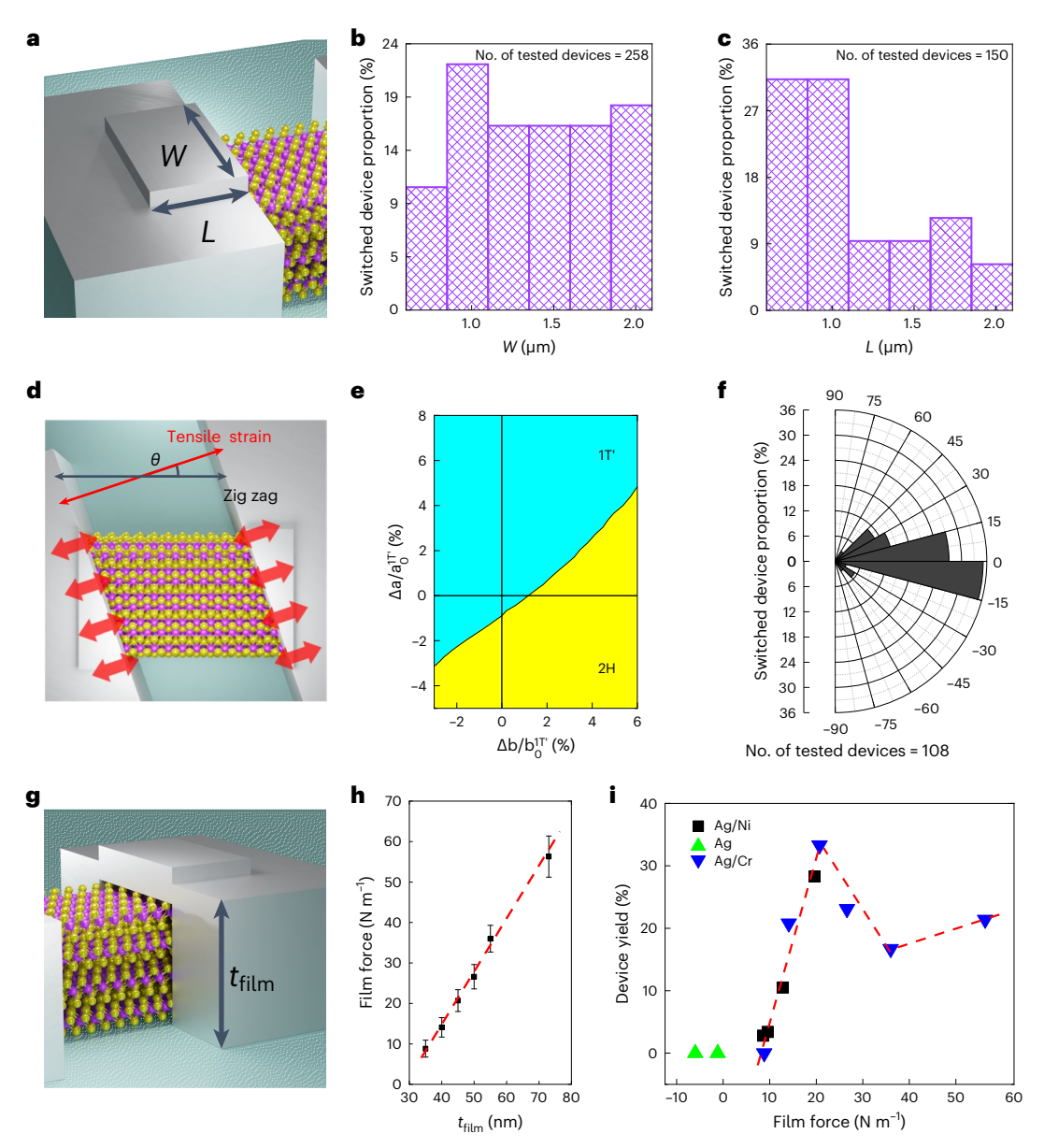


Fig. 3 | **Analysis of devices with respect to device parameters. a**, Schematic of the device highlighting variable contact length and contact width. **b,c**, Histogram showing the switched device proportion with different contact width and contact length. **d**, Schematic of the device with the angle of θ between contact edge-induced strain and the zigzag direction of the 1T'-MoTe₂ flake. **e**, Structural phase diagram of monolayer MoTe₂ obtained by DFT, from the phase stability point of 1T'-MoTe₂, where **a** is the lattice constant along the armchair direction of the 1T' phase and **b** is the lattice constant along the zigzag direction of the 1T' phase. The origin is placed at the unstrained pristine 1T'-MoTe₂ lattice constant in **a** and **b** lattice directions. $\Delta a/a_0^{1T}$ and $\Delta b/b_0^{1T}$ represent strain applied

from the equilibrium 1T' phase stability point along the armchair and zigzag directions, respectively. ${\bf f}$, Switched device proportion with contact edge-induced strain applied to different directions of the 1T'-MoTe₂ flake relative to the zigzag direction, represented by degrees from the zigzag axis. ${\bf g}$, Schematic of the device highlighting the contact thickness. ${\bf h}$, Film force of Ag/Cr bilayer film as a function of film thickness $t_{\rm film}$, where $t_{\rm film}$ is the total thickness of 25 nm Ag and x nm Cr. Data points are mean \pm standard error of the mean (s.e.m.) (n = 3). ${\bf i}$, Device yield under different film forces where there is a clear film force trend independent of contact metal composition.

We first tested the role of contact width W and contact length L (defined in Fig. 3a) by randomly varying W from 0.6 μ m to 2.1 μ m while keeping the film force of the contacts above 15 N m⁻¹ for all the devices. We made 258 devices in total and found 55 devices that started at the HRS, which we denote as 'switched devices'. As shown in Fig. 3b, we found the proportion of switched devices showing weak to no dependence on the contact width. Among the 258 devices, there are 150 devices that we also randomly varied in contact length L from 0.6 μ m to 2.1 μ m during fabrication. As shown in Fig. 3c, among these 150 devices, we found most switched devices having a contact length below 1.1 μ m. This is because the contact edge-induced strain

is localized near the edge, as demonstrated from the Raman profile in Fig. 2f. When the contact length is too long, only the region near the edge would switch phase by the applied strain and the device will still be shorted by the unswitched semimetallic 1T' region away from the edge, thereby exhibiting low resistance.

Through the previous analysis, we know to keep contact length <1 μ m to design for uniaxial tensile strain. Next, we then tested the role of angle θ between the edge-induced tensile strain and zigzag direction of the flake (defined in Fig. 3d), while keeping the contact geometry fixed. Due to the in-plane anisotropic nature of the 1T' phase of MoTe₂, to change it from the semimetallic phase to the semiconducting 2H

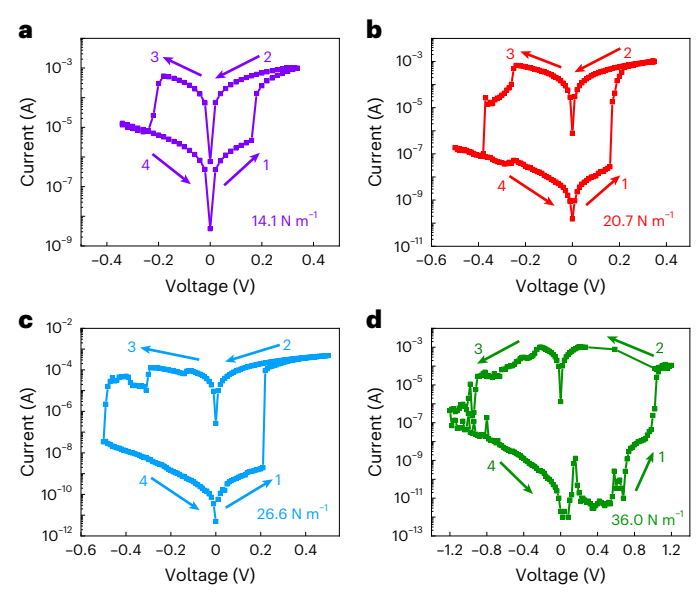


Fig. 4 | **Resistive switching under different film force.** $\bf a-d$, Typical $\bf I-V$ characteristic of devices under $\bf 14.1~N~m^{-1}(a)$, $\bf 20.7~N~m^{-1}(b)$, $\bf 26.6~N~m^{-1}(c)$ and $\bf 36.0~N~m^{-1}(d)$ film force. Numbering on plots $\bf (1,2,3,4)$ specifies the voltage sweeping sequence.

phase, it will require tensile strain applied along its zigzag direction, as shown in Fig. 3e, which we modelled using density functional theory (details can be found in Methods). Of the 258 devices we fabricated, 108 devices were deliberately made with contact length below 1 µm during the device fabrication. Within these devices, θ was randomly varied between -90° and 90° relative to the zigzag direction. Among these 108 devices, as shown in Fig. 3f, we found most switched devices had θ between -15° to 15°, which shows that the edge-induced tensile strain must be applied along the zigzag direction of the 1T'-MoTe₂ to switch it to the semiconducting state. This characteristic property can be better understood in light of the theoretical findings presented in Fig. 3e, which shows the structural phase map of the 1T'- and 2H-MoTe₂. The positioning of the unstrained 1T'-MoTe₂ relative to the 2H boundary line requires similar strain directions to cross the phase-change boundary. This strong angular dependence and the match with theoretical calculation strongly suggest that we are correctly inducing a strain-based phase change in our devices that is both applied and detected by the contact metal itself. We are assisted by the fact that our contact metals naturally provide both tensile strain perpendicular to the contact edge (zigzag) as well as compression parallel to the contact edge (armchair), which according to Fig. 3e is the fastest way to the phase boundary. More detailed analysis of individual strain component effects on phase change with respect to the calculated phase diagram is presented in Supplementary Figs. 7-14.

Finally, with an understanding of the nature of strain applied by the contact geometry, the effect of film force can be explored, which has been shown previously to be directly proportional to strain magnitude^{26,29}. Here, we the fixed tensile strain direction to the zigzag direction of the flake, ensured contact length *L* is below 1.1 µm for uniaxial tension, and varied film force of the contacts by changing contact thickness. New sets of devices with different values of film force from the metal contacts are fabricated, with over 25 devices in each set. It has shown that changing the thickness of the Ni layers can linearly control the film force in Ag/Ni bilayer films²⁹. Here, using the same method, we show we can also linearly control the film force in Ag/Cr bilayers, as shown in Fig. 3h. Based on this, we fabricated devices made from Ag, Ag/Ni bilayer or Ag/Cr bilayer films and characterized the percentage of devices starting in the HRS in each set of devices, which we defined as the device yield. From Fig. 3i, it is clear there is a film

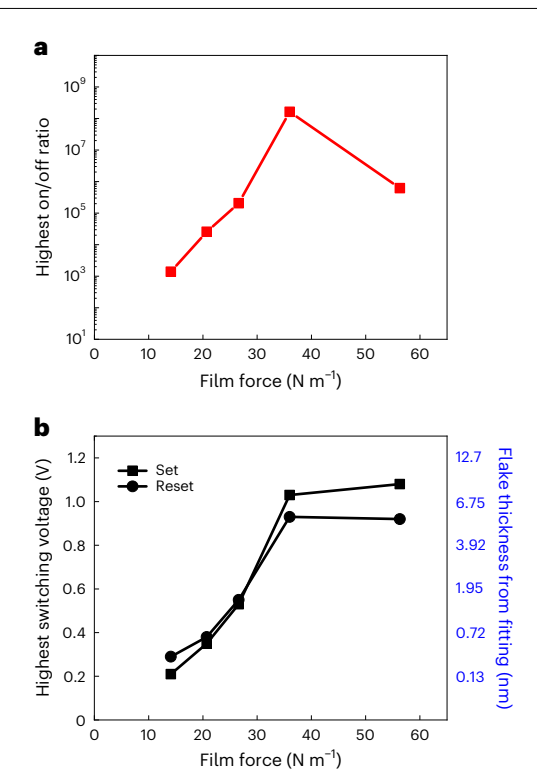


Fig. 5 | Film-force-controllable switching characteristic. a, Highest on/off ratio of devices under different film forces. b, Highest switching voltage of devices under different film forces and the corresponding extracted flake thickness assuming thickness scaling from previous $MoTe_2$ phase-change works¹², modelled by fitting previous results shown in Supplementary Fig. 5.

force and therefore strain magnitude dependence on the nature of the phase changes that occur under the contacts. The device yield stays at 0% when there is negative film force or low film force applied from the contacts, up to some threshold value. When the film force is larger than 10 N m⁻¹, the device yield first linearly increases with the film force and peaks around 21 N m⁻¹. When the film force further increases, the device yield starts to drop and then increases again, as the strain is too large and strain solitons begin to form^{33,34}. This is a well-known characteristic of strained 2D materials, where layers begin to slip or ripple on top of each other, before latching on again, producing a sawtooth-like pattern for strain transferred. Looking at other works on the topic 33,34, there is an almost one-to-one relation between our device yield curve and the predicted results of strain transferred given applied stress including soliton formation. This further strengthens the concept that strain from the contacts are generating an active semiconducting region for a self-aligned vertical transport memristor.

Memristive switching characterization

Once all variables in the previous section are controlled, we explore the current–voltage (I-V) characteristics of each of the switched devices. These results are presented in Fig. 4a–d, where each device starting in the HRS exhibits bipolar memristive switching, which occurs without any forming procedure. From the same sets of devices used for film force characterization, we also found the device switching characteristics can be controlled by the film force. Both the on/off ratio and the switching voltage change with film force applied from the metal contacts. This is understood as higher film force contacts causing higher on/off ratios because more layers and therefore a larger region of the flake were switched to the semiconducting state under the application of larger strain by the contacts. This increasing of the thickness of the active region under the contact makes the HRS of the device less conducting. The highest switching voltage of the device also tends to

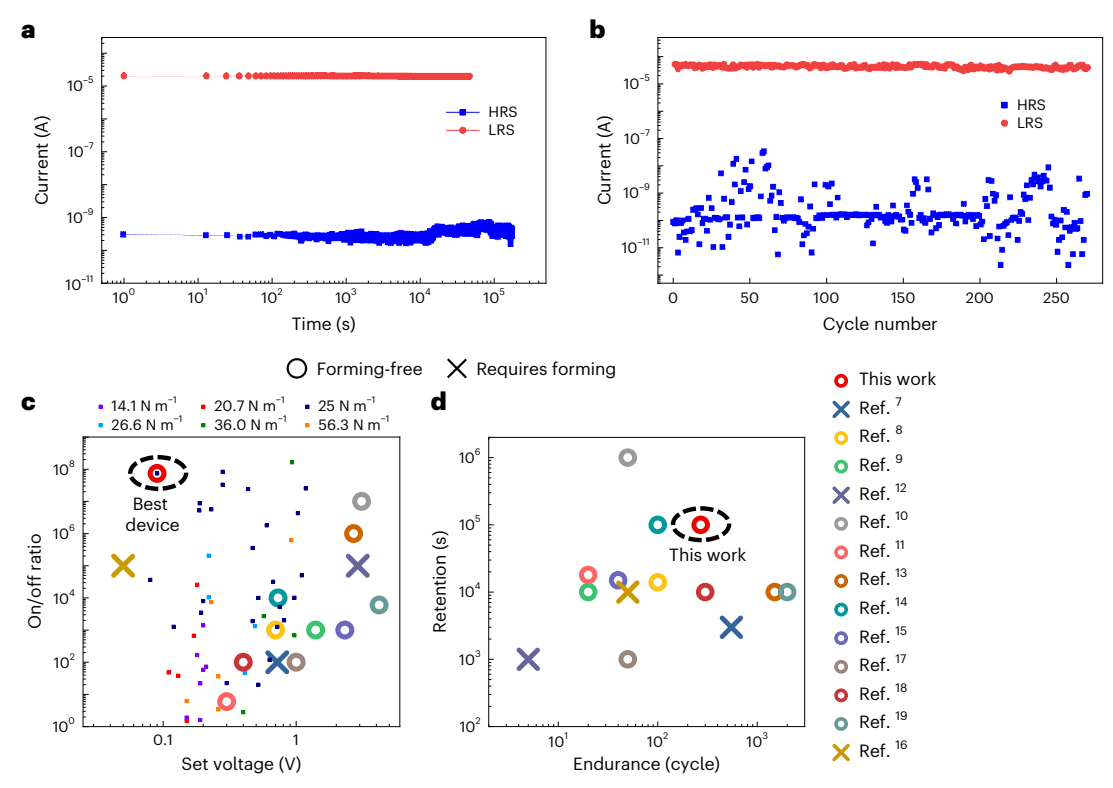


Fig. 6 | **Strain-based 1T' MoTe₂ memristor performance. a**, Retention of strain-based 1T'-MoTe₂ memristor over 10^5 s. **b**, Endurance of strain-based 1T'-MoTe₂ memristor with over 270 manual DC switch cycles. **c**, Comparison of on/off ratio and set voltage of all fabricated devices labelled by film force (filled squares) to

highest performing 2D memristors (open circles and crosses). **d**, Comparison of retention and endurance of highest performing 2D memristors. Full comparison is shown in Supplementary Table 1.

increase under higher film force, because as more layers of the flake have switched phase by the strain, a larger voltage is required to reach the same electric field needed for the electric-field-induced phase transition. Although we note that the highest switching voltage is not representative of the average switching voltages observed in our work, which tend to be lower since strain is used to bring the devices closer to the phase transition boundary. For example, for the device presented in Fig. 4c, the switching voltage is 210 mV for a relatively high on/off ratio of 1.4×10^5 . A more detailed summary of the relationship of switching voltage and on/off ratio for all devices fabricated is presented in the next section.

We found that there is statistical variation in each set of the devices, as shown in Supplementary Fig. 4. This is due to uncontrolled device parameters during the fabrication, for example, the shape of exfoliated flakes, which will greatly affect the profile of the strain. As we are using as-exfoliated thin flakes of MoTe₂, only contact metal overlap with the flake can be controlled and therefore there will be variation in the device performance due to this and other uncontrolled device fabrication variables. When just the highest on/off ratio and the highest switching voltage are extracted from each set of devices, the device performance (switching voltage, on/off ratio) clearly scales with the film force we applied in each set (Fig. 5a, b). The highest on/off ratio increases with film force, and eventually reaches over 108, and subsequently decreases because the strain is too large and some regions of the flake are stuck in the semiconducting state and cannot be switched back to the semimetallic state by the electric field. This causes the LRS in these devices to become less conducting. The highest switching voltage increases with film force and eventually plateaus around 1.1 V. By fitting the data from the previous 2H-MoTe₂ memristor work¹² (Supplementary Fig. 5), we extracted the relation between the switching voltage and the active region thickness, which shows that the 1.1 V switching voltage corresponds to a flake thickness around ~7 nm (Fig. 5b). This matches with

the out-of-plane strain transfer length scale in Fig. 2c, showing there is maximally -7 nm of the flake that can be switched under high film force. This shows that our expectation of how strain is transferred based on Raman spectroscopic analysis matches device performance, further validating our strain-based phase-change mechanism that drives device design. A more detailed discussion to exclude other possible switching mechanisms in our devices other than the strain-based phase switching is provided with Supplementary Fig. 6.

We note that while the highest on/offratio represents the best-case scenario devices of each set, the highest switching voltage represents the worst-case scenario devices since it matches the expectation of the original phase-change memristor result without strain enhancement. The average behaviour of our devices has a switching voltage far lower than the maximum worst-case scenario, which is presented as a validity check to the original result. The next section will present in more detail how the on/off ratio and switching voltage are not negatively linked, and how further strain engineering may lead to more uniform high performance in devices.

Device performance

To further understand the performance of these devices, both retention and endurance were tested, with typical results shown in Fig. 6a,b. LRS and HRS maintained state for longer than 10^5 s at room temperature and over 270 times DC cycling (Fig. 6a,b). Note that for endurance testing, only I-V curves that the ensured successful switching of the device in every cycle are taken into account 35 . Similarly, devices were tested for switching time where non-volatile device switching was demonstrated with voltage pulses as short as 5 ns with an estimated switching energy, $E_{\text{switch}} = I_{\text{LRS}} \times V_{\text{switch}} \times t_{\text{switch}} = 150$ aJ (Supplementary Fig. 19), where I_{LRS} is the current in the low resistance state, V_{switch} is the switching voltage, and t_{switch} is the switching time. To benchmark the overall performance of our devices, a comparison of device performance metrics between

this work and other recent 2D memristors⁷⁻¹⁹ are given in Fig. 6c,d. All devices fabricated within this work are presented and compared to the highest performing single device of each of the 2D memristor works in Fig. 6c. As can be seen, while device variability may still be high due to uncontrolled exfoliated flake geometries, nearly all devices fabricated either match or outperform previously reported 2D memristors. Our devices, with switching voltages as low as 90 mV, on/off ratios over 10⁸, retention longer than 10⁵ s, endurance over 270 cycles and forming-free switching, show that within a single implementation we improved the on/off ratio and switching voltage by several orders of magnitude compared to reported 2D memristive devices without forming. Our best single device is highlighted (red circle) in Fig. 6c with a combined 90 mV switching voltage and 7.4×10^7 on/ off ratio (the full I-V characteristics are presented in Supplementary Fig. 15). Endurance and retention are also moderately high in comparison to other recent works. When compared to the original phase-change MoTe₂ memristor result (Fig. 6c,d, purple cross), our strain-engineering implementation has enhanced all four metrics (on/off ratio, switching voltage, endurance and retention) by several orders of magnitude, providing strain-engineering based enhancement in the same way strain engineering was used to enhance the performance of conventional silicon-based metal-oxide-semiconductor field-effect transistors. A more detailed comparison for all performance metrics in recent 2D memristors is given in Supplementary Table 1.

As we have changed the mechanism of memristive switching in our implementation away from filamentary conduction, it implies that there may also be a change in device area scaling. Incurring larger switching voltages or requiring larger forming voltages as the device area becomes smaller is a critical limitation in the commercial implementation of memristive memories³⁶. This arises since smaller area devices have less chances to encounter defects to seed filamentary conductivity. Within our set of fabricated phase-change memristors, we see that switching voltage does not increase with a decreasing device area, suggesting the validity of the phase-change memristor concept (Supplementary Fig. 17). It appears that as device area becomes smaller, switching voltage may actually become more predictable, with smaller area devices likely having more uniform strain distributions.

Compared to traditional transition metal oxide-based memristors, although higher device endurance (>109) has been demonstrated, they also require higher switching voltage (~1 V) and have lower switching speeds because of the filamentary switching mechanism and the thicker active layer to prevent current leakage^{37,38}. Our device, with a 2D active layer and a phase-switching mechanism, enables much lower switching voltage and high switching speeds. Endurance may be improved after further device engineering as phase switching is less prone to defect-induced device breakdown compared to filamentary switching³⁹. Similarly, other limiting factors may be further explored through modelling and simulation of strain-induced phase changes, such as understanding ideal strain profiles through control of flake geometries and ideal strain magnitudes to maximize device starting state. Since the mechanism of memristive switching is entirely different, the limitations of previous classes of memristive devices may not be relevant, but further work is needed to understand the upper performance limit of phase-change memristive devices in general.

Conclusions

We have reported a strain-based 1T'-MoTe₂ memristor with high overall device performance. Strain-induced and electric-field-induced phase transitions of MoTe₂ are used together, with the former setting the initial semiconducting active region and the latter achieving the reversible resistive switching behaviour. Though both types of phase transition in MoTe₂ have been experimentally reported ^{12,24}, the effect is compounded when used together. The contact geometry

dependence and the strain direction dependence of the device starting state is shown to match the strain profile of the flake. The tuneable device switching characteristics by the film force illustrates the high engineering potential of this strain-based memristor. Further optimization of strain-engineered phase-change memristors could provide a route to robust, fast, low power and scalable applications in non-volatile memories, in-memory computing and neural-network based neuromorphic computing.

Methods

Device fabrication

For all devices, MgO substrates with polished surfaces (Ra < 0.5 nm) were oxygen plasma cleaned at 100 W and 200 mTorr for 20 min. The reactive ion chamber was also cleaned by oxygen plasma for 25 min before the substrate was put in to ensure that no contaminants can be redeposited onto the MgO surface⁴⁰. Substrate prepreparation matters greatly in ensuring high adhesion of the MoTe₂ flake to the substrate, a critical parameter in ensuring predictable strain profiles. Right after the plasma cleaning (<1 min), commercially purchased 1T'-MoTe₂ (HQ Graphene) was exfoliated onto the pretreated MgO substrate using Scotch tape, and the substrate was baked at 100 °C for 90 s with the tape still in contact. The tape was slowly removed after the heating procedure is completed. It should be pointed out that all flakes were exfoliated by the tape from one rectangular-shaped 1T'-MoTe₂ crystal, with the long edge of the crystal along its zigzag direction. When the exfoliation was completed, flakes on the substrate showed a preferred cleavage direction along that long edge of the bulk crystal, which is the zigzag direction, confirmed by polarized Raman spectroscopy. We then test substrate adhesion through ultrasonic bath delamination threshold testing⁴⁰ by placing the MgO substrate in an acetone and then isopropanol ultrasonic bath for 30 min and 5 min respectively to remove the flakes on the substrate surface with poor adhesion. Optical contrast was then used to identify the rest of the flakes with thickness in the 7 nm to 25 nm range on the substrate. Ag, Ag/Ni bilayers (25 nm Ag with various thickness Ni on top), Ag/Cr bilayers (25 nm Ag with various thickness Cr on top), or Cr/Au bilayers (various thickness Cr with 20 nm Au on top) contacts were then patterned for lift-off on the flakes using direct-write laser photolithography using a Microtech LW405 laserwriter system and S1805 photoresist. All metals are deposited using e-beam evaporation under a chamber pressure below 2×10^{-5} torr at a rate of 1 Å s⁻¹. Vacuum condition is maintained throughout the whole deposition process.

Film force characterization

Metal thin films are deposited onto cleaned microscope coverslips using the same evaporation conditions as the fabrication of the MoTe₂ memristors. The radius of curvature of the coverslips before and after the deposition are measured using contact profilometry. The average film stress, $\bar{\sigma}$, can then be calculated from the Stoney equation²⁹. The applied film force $F_{\rm f}$, that is, force per unit width, is obtained through $F_{\rm f} = t_{\rm f} \times \bar{\sigma}$, where $t_{\rm f}$ is the thickness of the metal thin film.

Device characterization

For *I–V* characteristics, the devices were measured by a Keysight 2901 A Precision Source/Measure Unit (SMU) with a current compliance of 1–2 mA in air. For retention testing, the current was measured every 10 s under 50 mV using the same SMU. For endurance testing, sequences of full *I–V* sweeps of the device were collected using the same SMU to make sure the device switched in every cycle³⁵. The current at 100 mV in every cycle was extracted in Fig. 6b. The retention and endurance tests were conducted in a helium gas protected environment to prevent the device from degrading. For switching speed test, a Highland Technology P400 pulse generator and Cascade Microtech Summit 12000 RF probe station was used. All measurements were performed at room temperature.

Raman spectroscopy

All MoTe₂ samples for Raman spectroscopy were exfoliated on MgO substrates in the same way as memristor devices. For samples of single-point Raman measurements, the optically transparent stressor made of 5 nm Ti or 10 nm Al₂O₃, 100 nm MgF₂ and 10 nm Al₂O₃ was e-beam evaporated to uniformly cover flakes with different thicknesses. The bottom layer of Ti was deposited at the rate of 0.1 Å s^{-1} and the bottom Al_2O_3 was deposited at 1 Å s^{-1} . Then the MgF₂ and Al₂O₃ layers were deposited at the rate of 2 Å s^{-1} and 1 Å s^{-1} , respectively. The chamber pressure was kept below 2×10^{-5} torr throughout the deposition. Both films (5 nm Ti/100 nm MgF₂/10 nm Al_2O_3 and 10 nm $Al_2O_3/100$ nm $MgF_2/10$ nm Al_2O_3) were measured to have a 55 N m⁻¹ film force. Uniformly covered MoTe₂ flakes with various thicknesses were then studied with single-point Raman microscopy with a 532 nm, 0.5 mW laser. Raman peak shift due to strain was measured by comparing covered flakes to uncovered flakes of the same thickness, using the trend in peak position of uncovered flakes as a reference.

For samples of Raman line-scan measurements, patterned stressors (5 nm Ti/20 nm MgF $_2$ /10 nm Al $_2$ O $_3$) containing a 10 N m $^{-1}$ film force were deposited onto 1T' flakes with a 10 nm thickness to partially cover the flakes, so that the stressor edge was perpendicular to the zigzag direction of the flake. Deposition conditions were the same as the samples for single-point Raman measurements. Raman line scans were performed along the direction that is perpendicular to the stressor's edge. The laser power was kept below 1 mW to prevent laser induced damage to the flakes. The strain profile was also studied in a second set of MoTe $_2$ (8–11 nm thick) samples partially covered by the stressor (5 nm Ti/50 nm MgF $_2$ /10 nm Al $_2$ O $_3$) with film force of 30 N m $^{-1}$, which showed a similar strain profile to the samples with lower film force. All Raman peaks were fitted by Lorentzian functions.

DFT calculation of phase diagram

We performed density functional theory (DFT) simulations using the open-source Quantum Espresso package within the generalized gradient approximation (GGA) scheme utilizing projector-augmented waves (PAW) pseudopotentials⁴¹. The Perdew-Burke-Ernzerhof (PBE) form along with GGA was used as the exchange-correlation functional⁴². Total energies of the structures were converged by expanding the wavefunctions in a plane wave basis setup to an energy cutoff and charge density of 45 Ry and 400 Ry respectively. We used a $20 \times 10 \times 1$ k-point mesh generated by Monkhorst-Pack to sample the reciprocal space. The systems were considered relaxed until all the atomic forces were less than $0.01 \text{ eV } \text{Å}^{-1}$. Initially, the ground state configurations of the monolayer 1T' and 2H-MoTe₂ structures were obtained from their DFT optimized rectangular lattice parameters (a = 6.388 Å, b = 3.445 Å for 1T' and a = 6.146 Å, b = 3.549 Å for 2H).A vacuum spacing of 25 Å is considered along the out-of-plane caxis to avoid spurious interactions between periodic images in that direction.

To capture the phase transition boundary between 1T' and 2H phases as a function of uniaxial strain, their respective a and b lattice constants were varied followed by the calculation of total energies of the strained systems. While relaxing the structures in the presence of strain, the lattice constant along the strained direction is fixed at a given strain value, while that along the transverse direction is fully relaxed along with the inner atomic coordinates. The applied uniaxial strain (ε) is expressed as $\varepsilon = \frac{l-l_0}{l_0}$, where l and l_0 are the respective lattice constants of strained and pristine MoTe $_2$ structures. On calculating the total energies as a function of lateral lattice constants produces a phase diagram for monolayer 1T'/2H-MoTe $_2$. The energy surface intersection contour plot of the two phases with respect to percentage engineering strain in Fig. 3e shows that 1T' to 2H transition occurs at 1.2% strain along b lattice for monolayer (zigzag direction), in agreement with earlier work 43 .

Data availability

Source data are provided with this paper. All other data that support the findings of this study are available from the corresponding author upon reasonable request.

References

- Chua, L. Memristor-the missing circuit element. *IEEE Trans. Circuit Theory* 18, 507–519 (1971).
- Strukov, D. B., Snider, G. S., Stewart, D. R. & Williams, R. S. The missing memristor found. *Nature* 453, 80–83 (2008).
- Xia, Q. F. & Yang, J. J. Memristive crossbar arrays for brain-inspired computing. *Nat. Mater.* 18, 309–323 (2019).
- Yang, J. J. S., Strukov, D. B. & Stewart, D. R. Memristive devices for computing. *Nat. Nanotechnol.* 8, 13–24 (2013).
- Duan, H. et al. Low-power memristor based on two-dimensional materials. J. Phys. Chem. Lett. 13, 7130–7138 (2022).
- Huh, W., Lee, D. & Lee, C. H. Memristors based on 2D materials as an artificial synapse for neuromorphic electronics. *Adv. Mater.* 32, 2002092 (2020).
- Qian, K. et al. Hexagonal boron nitride thin film for flexible resistive memory applications. Adv. Funct. Mater. 26, 2176–2184 (2016).
- 8. Zhao, H. et al. Atomically thin femtojoule memristive device. *Adv. Mater.* **29**, 1703232 (2017).
- 9. Kim, M. et al. Zero-static power radio-frequency switches based on MoS₂ atomristors. *Nat. Commun.* **9**, 2524 (2018).
- Wu, X. H. et al. Thinnest nonvolatile memory based on monolayer h-BN. Adv. Mater. 31, 1806790 (2019).
- 11. Xu, R. J. et al. Vertical MoS_2 double-layer memristor with electrochemical metallization as an atomic-scale synapse with switching thresholds approaching 100 mV. *Nano Lett.* **19**, 2411–2417 (2019).
- Zhang, F. et al. Electric-field induced structural transition in vertical MoTe₂- and Mo_{1-x}W_xTe₂-based resistive memories. *Nat. Mater.* 18, 55–61 (2019).
- Chen, S. C. et al. Wafer-scale integration of two-dimensional materials in high-density memristive crossbar arrays for artificial neural networks. *Nat. Electron.* 3, 638–645 (2020).
- Li, Y. S. et al. Anomalous resistive switching in memristors based on two-dimensional palladium diselenide using heterophase grain boundaries. *Nat. Electron.* 4, 348–356 (2021).
- Liu, L. et al. Low-Power memristive logic device enabled by controllable oxidation of 2D HfSe₂ for In-Memory computing. Adv. Sci. 8, 2005038 (2021).
- Lei, P. X. et al. High-performance memristor based on 2D Layered BiOI nanosheet for low-power artificial optoelectronic synapses. Adv. Funct. Mater. 32, 2201276 (2022).
- Pam, M. E. et al. Interface-modulated resistive switching in mo-irradiated res₂ for neuromorphic computing. *Adv. Mater.* 34, 2202722 (2022).
- Yin, L. et al. High-performance memristors based on ultrathin 2D copper chalcogenides. Adv. Mater. 34, 2108313 (2022).
- Zhang, X. L. et al. Tunable resistive switching in 2D MXene Ti₃C₂ nanosheets for non-volatile memory and neuromorphic computing. ACS Appl. Mater. Interfaces 14, 44614–44621 (2022).
- 20. Zhang, F. et al. An ultra-fast multi-level MoTe₂-based RRAM. In *IEEE Int. Electron Devices Meet.* **22**, 22.7.1–22.7.4 (IEEE, 2018).
- 21. Duerloo, K. A. N., Li, Y. & Reed, E. J. Structural phase transitions in two-dimensional Mo- and W-dichalcogenide monolayers. *Nat. Commun.* **5**, 4214 (2014).
- Orain, S., Fiori, V., Villanueva, D., Dray, A. & Ortolland, C. Method for managing the stress due to the strained nitride capping layer in MOS transistors. *IEEE Trans. Electron Devices* 54, 814–821 (2007).

- Thompson, S. E., Sun, G. Y., Choi, Y. S. & Nishida, T. Uniaxial-process-induced strained-Si: extending the CMOS roadmap. IEEE Trans. Electron Devices 53, 1010–1020 (2006).
- Hou, W. et al. Strain-based room-temperature non-volatile MoTe₂ ferroelectric phase change transistor. *Nat. Nanotechnol.* 14, 668–673 (2019).
- 25. Azizimanesh, A., Pena, T., Sewaket, A., Hou, W. H. & Wu, S. M. Uniaxial and biaxial strain engineering in 2D MoS₂ with lithographically patterned thin film stressors. *Appl. Phys. Lett.* **118**, 213104 (2021).
- 26. Pena, T. et al. Strain engineering 2D MoS_2 with thin film stress capping layers. 2D Mater. **8**, 045001 (2021).
- Pena, T. et al. Temperature and time stability of process-induced strain engineering on 2D materials. J. Appl. Phys. 131, 024304 (2022).
- Chowdhury, S. A. et al. Mechanical properties and strain transfer behavior of molybdenum ditelluride (MoTe₂) thin films. J. Eng. Mater. Technol. 144, 011006 (2022).
- 29. Hou, W. H. et al. Nonvolatile ferroelastic strain from flexoelectric internal bias engineering. *Phys. Rev. Appl.* **17**, 024013 (2022).
- 30. Wang, J. Y. et al. Determination of crystal axes in semimetallic T'-MoTe_2 by polarized Raman spectroscopy. *Adv. Funct. Mater.* **27**, 1604799 (2017).
- 31. Kan, M., Nam, H. G., Lee, Y. H. & Sun, Q. Phase stability and Raman vibration of the molybdenum ditelluride (MoTe₂) monolayer. *Phys. Chem. Chem. Phys.* **17**, 14866–14871 (2015).
- Zhang, Y. J. et al. Mechanical properties of 1T-, 1T '-, and 1H-MX₂ monolayers and their 1H/1T '-MX₂ (M = Mo, W and X = S, Se, Te) heterostructures. AIP Adv. 9, 125208 (2019).
- Kim, S. et al. Stochastic stress jumps due to soliton dynamics in two-dimensional van der waals interfaces. Nano Lett. 20, 1201–1207 (2020).
- Kumar, H., Dong, L. & Shenoy, V. B. Limits of coherency and strain transfer in flexible 2D van der Waals heterostructures: formation of strain solitons and interlayer debonding. Sci Rep. 6, 21516 (2016).
- Lanza, M. et al. Recommended methods to study resistive switching devices. Adv. Electron. Mater. 5, 1800143 (2019).
- Lanza, M., Molas, G. & Naveh, I. The gap between academia and industry in resistive switching research. Nat. Electron. 6, 260–263 (2023).
- Yang, J. J. et al. High switching endurance in TaO_x memristive devices. Appl. Phys. Lett. 97, 232102 (2010).
- Lee, M. J. et al. A fast, high-endurance and scalable non-volatile memory device made from asymmetric Ta₂O_{5-x}/TaO_{2-x} bilayer structures. Nat. Mater. 10, 625–630 (2011).
- Raoux, S., Welnic, W. & Ielmini, D. Phase change materials and their application to nonvolatile memories. *Chem. Rev.* 110, 240–267 (2010).
- Pena, T., Holt, J., Sewaket, A. & Wu, S. M. Ultrasonic delamination based adhesion testing for high-throughput assembly of van der Waals heterostructures. J. Appl. Phys. 132, 225302 (2022).
- Scandolo, S. et al. First-principles codes for computational crystallography in the Quantum-ESPRESSO package.
 Kristallogr. 220, 574–579 (2005).

- 42. Perdew, J. P., Burke, K. & Ernzerhof, M. Generalized gradient approximation made simple. *Phys. Rev. Lett.* **77**, 3865–3868 (1996).
- 43. Sun, Y. F. et al. Low-temperature solution synthesis of few-Layer 1T'-MoTe₂ nanostructures exhibiting lattice compression. *Angew. Chem. Int. Ed.* **55**, 2830–2834 (2016).

Acknowledgements

S.M.W. acknowledges support from the National Science Foundation (OMA-1936250 and ECCS-1942815). Raman spectroscopy was performed at the Cornell Center for Materials Research Shared Facilities (CCMR), and CCMR is supported through the NSF MRSEC Program (No. DMR-1719875). We would like to thank Qiang Lin at the University of Rochester in aiding us with the equipment that made it possible to obtain switching speed test results.

Author contributions

The device fabrication was performed by W.H. and A.A. and the device characterization was performed by W.H., Y.Y. and C.S. Raman spectroscopy was performed by A.A. Thin film stress measurements were performed by W.H. and A.A. The density functional theory simulation of the strain phase diagram was performed by A.D. and supervised by H.A. and S.S. High-speed pulse testing was performed by W.H. and W.W., and supervised by H.W. Figure rendering was performed by W.H. and the paper was written by W.H., A.A. and S.M.W. Original experiment conception and project supervision was provided by S.M.W.

Competing interests

The authors declare no competing interests.

Additional information

Supplementary information The online version contains supplementary material available at https://doi.org/10.1038/s41928-023-01071-2.

 $\begin{tabular}{ll} \textbf{Correspondence and requests for materials} should be addressed to Stephen M. Wu. \end{tabular}$

Peer review information *Nature Electronics* thanks Ning Dai, Jianhua Hao and Huairuo Zhang for their contribution to the peer review of this work.

Reprints and permissions information is available at www.nature.com/reprints.

Publisher's note Springer Nature remains neutral with regard to jurisdictional claims in published maps and institutional affiliations.

Springer Nature or its licensor (e.g. a society or other partner) holds exclusive rights to this article under a publishing agreement with the author(s) or other rightsholder(s); author self-archiving of the accepted manuscript version of this article is solely governed by the terms of such publishing agreement and applicable law.

@ The Author(s), under exclusive licence to Springer Nature Limited 2023